Journal of Magnetic Resonance **139,** 67–73 (1999)
Article ID jmre.1999.1747, available online at http://www.idealibrary.com on IDEAL®

Selective Imaging of Biofilms in Porous Media by NMR Relaxation

Brian C. Hoskins,* Liv Fevang,* Paul D. Majors,* Mukul M. Sharma,* and George Georgiou†

*Department of Petroleum and Geosystems Engineering, The University of Texas at Austin, MC C0300 Building CPE 2.502, and
†Department of Chemical Engineering, The University of Texas at Austin, MC C0400 Building CPE 2.802, Austin, Texas 78712

Received June 19, 1998; revised December 29, 1998

Nuclear magnetic resonance imaging (NMRI) techniques were employed to identify and selectively image biological films (biofilm) growing in aqueous systems. Biofilms are shown to affect both the longitudinal (T_1) and transverse (T_2) NMR relaxation time values of proximal water hydrogens. Results are shown for biofilm growth experiments performed in a transparent parallel-plate reactor. A comparison of biofilm distributions by both NMR and optical imaging yielded general agreement for both an open-flow system and an idealized porous system (the reactor without and with packed glass beads, respectively). The selective imaging of biofilm by relaxation NMRI is dependent upon the resolution of relaxation times for the fluid phases, dynamic range, and signal-to-noise ratio. For open-flow systems, the use of a rapid and quantitative T_2-sorted NMRI technique was preferred. For porous systems where T_2 values are generally more similar, a T_1-weighted technique was preferred.

Key Words: **biofilm; porous media; selective imaging; relaxation NMRI; image sorting.**

INTRODUCTION

Biological remediation processes in trickling filters, porous bioreactors, and soils rely on agent growth and formation. Most of the biomass is in the form of a biological film or biofilm, i.e., microorganism colonies anchored to the medium surface by excreted saccharide polymers (*1*). In porous systems, hydraulic conductivity, pore velocity distribution, biofilm thickness, and surface roughness affect the delivery rate of nutrients and reactants to growing cells (*2*), and thus the rate of bioremediation. Quantitation of the processes controlling transport will lead to a better understanding of the kinetics of biotransformation, microbial growth, and the ecology of active microorganisms.

Experimental studies of biofilms in porous media typically use columns packed with sand, glass beads, or soil material (*2–4*). The concentration of free cells in the pore fluid may be determined from fluid samples, but the amount and spatial distribution of biofilm must be found by dismantling the columns and assaying their contents for organic carbon (*3*). Thus, a nondestructive assay is needed to specifically monitor the concentration of surface-attached cells *in situ.*

Nuclear magnetic resonance (NMR) has been used in a variety of ways to study bacteria and biofilms. Brownstein and Tarr (*5*) used NMR relaxometry of water molecules to study diffusion in biological cells. Pettegrew (*6*) studied the effects of cell size and shape upon NMR relaxation decay characteristics.

NMR imaging (NMRI) techniques provide a nondestructive method of assessing biofilm growth. Lewandowski *et al.* (*7–10*) employed NMRI to image velocity fields surrounding biofilms growing in an open flow bioreactor. Potter *et al.* (*11*) demonstrated a one-dimensional NMRI method based on NMR diffusion measurements for assaying bacteria in a 0.2-ml quartz sand pack. This method yields spatially resolved bacterial cell concentrations, but requires the use of strong diffusion gradients (~75 G/cm). Stepp *et al.* (*12*) used NMR microscopy difference imaging to identify the boundary between biofilm and pore wall surfaces in a 5 × 7 mm sand pack.

In this study, we demonstrate the application of relaxation NMRI techniques for the selective imaging of biofilms in aqueous (nonporous and porous) systems. Biofilm identification was validated by performing experiments in transparent bioreactors.

BACKGROUND

Biofilms are known to reduce both the longitudinal (T_1) and the transverse (T_2) NMR relaxation time values of proximal water hydrogens (*5*). This observation is consistent with the biofilm surface impeding the motion of proximal water molecules, thereby enhancing NMR relaxation (*13*). This surface-induced reduction of NMR T_1 and T_2 values is also observed for fluid in porous media (*14*). The biofilm-associated signal derives primarily from intracellular and extracellular water hydrogens close to the film, enhancing sensitivity for biofilm detection.

NMRI is inherently influenced by NMR T_1 and T_2 relaxation times. For two weakly interacting fluid phases (a and b) with one resonance per phase and TR ⩾ TE, the local NMRI intensity $I(x, y)$ is described by

$$I(x, y) = I_{0a}(x, y)[1 - e^{\{-\mathrm{TR}/T_{1a}(x,y)\}}][e^{\{-\mathrm{TE}/T_{2a}(x,y)\}}] + I_{0b}(x, y)[1 - e^{\{-\mathrm{TR}/T_{1b}(x,y)\}}][e^{\{-\mathrm{TE}/T_{2b}(x,y)\}}], \quad [1]$$

1090-7807/99 $30.00

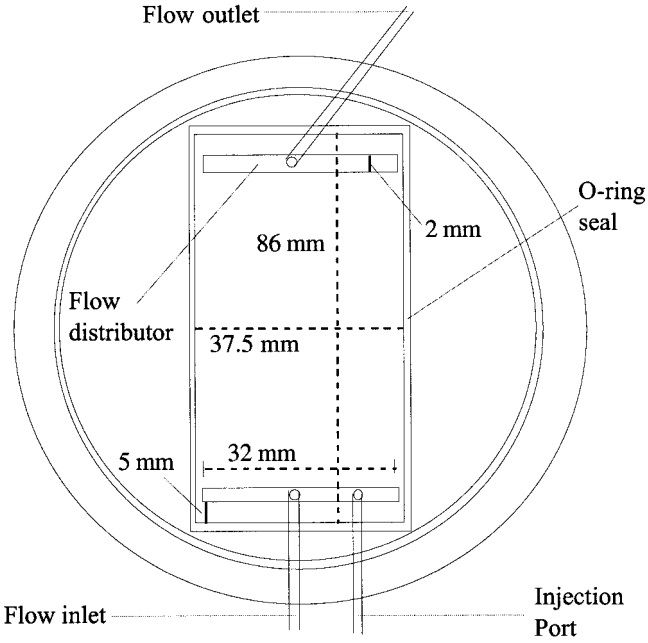

FIG. 1. Schematic drawing of the transparent parallel-plate bioreactor used in bioreactor growth experiments.

where $I_{0a}(x, y)$ is the total intensity (proportional to the concentration of nuclei) and $T_{1a}(x, y)$ and $T_{2a}(x, y)$ are the spatially resolved relaxation times for phase a. The T_1 and T_2 *weighting* terms in Eq. [1] are controlled by separate experiment variables, the subinterval repetition time TR and the echo time TE, respectively (*15*).

The selective imaging of the biofilm-associated water phase via *relaxation-weighted* NMRI is effective if there is an order-of-magnitude or larger difference in T_1 or T_2 between the fluid phases. A more reliable and quantitative approach is to employ *relaxation NMRI* methods (*16*), i.e., the acquisition of multiple, variably relaxation-weighted images $I(x, y)$, followed by attenuation analysis to indirectly determine the total intensities $I_0(x, y)$ and either $T_1(x, y)$ or $T_2(x, y)$. A relaxation model (exponential, biexponential, etc.) that adequately describes the data is employed. For T_2 NMRI, the resultant $I_0(x, y)$ intensities are corrected for T_2 relaxation and are therefore quantitative.

EXPERIMENTAL

Bioreactor growth studies. Biofilm growth experiments were performed in a transparent parallel-plate bioreactor (Fig. 1). The bioreactor was constructed from two 1.27-cm-thick pieces of Plexiglas. The flow channel (8.6 cm length × 3.75 cm width × 0.3 cm depth), O-ring groove, flow distributors, and flow connectors were cut into one of the Plexiglas pieces. The flow channel was sealed by securing the remaining Plexiglas piece on top of a Viton O-ring using four Teflon screws. Distributors (troughs 32 mm long and 2 mm wide placed 5 mm from each end of the flow channel) helped to provide a linear flow across the bioreactor. The fluid inlet, outlet, and an injection port were connected at the distributors. Nutrient flow was introduced through the inlet and outlet ports, while bacteria were introduced through the injection port. In a second reactor (schematic not shown), the flow connections were attached directly through the top plate.

The bioreactor was saturated with nutrient and then inoculated with 3 ml of *Escherichia coli*-enriched nutrient. The bacterial suspension was allowed to stand inside the bioreactor for 1 h. Subsequently, the nutrient flow (1.04 ml/min rate) was restarted and continued until a visible amount of biofilm had grown, approximately 5 days. The bioreactor was transferred to the test section of the NMR imager, and images were obtained. After NMR imaging, the sample was transported to another laboratory where photographs were obtained (Nikon FM2 35-mm camera with a Tamron 90-mm lens) and later digitized for a comparison with the NMR images.

The experiments were repeated with the bioreactor packed with 1.0- to 1.5-mm glass beads. The flow rate was reduced to 0.44 ml/min (minimum pump setting) to reduce shear stresses acting on the biofilm. After growth and NMRI experiments, the bioreactor was flooded with an immersion oil with the same refractive index as the glass beads, rendering the glass beads transparent and leaving the biofilm as the only visible material. Photographs of the bioreactor were obtained and digitized for comparison with NMRI.

NMR experiments. All NMR experiments were performed using a Unity SIS85/310 imaging spectrometer (Varian NMR Instruments, Palo Alto, CA) operating at a ^{1}H resonance frequency of 85.492 MHz. A 5-in.-diameter "saddle" RF coil served for both signal excitation and detection. The imaging *field of view* was 8 by 16 cm with a 2-cm slice thickness and yielded a top-down view of the model bioreactor. Two hundred fifty-six frequency-encoding steps were sampled in the flow direction, and 128 phase-encoding steps were performed in the lateral direction, yielding 0.62-mm pixel resolution in each direction. T_1-weighted spin-warp two-dimensional Fourier transform (conventional 2DFT) NMRI (*17*) experiments employed sixty-four 1-s repetitions (TE = 10 ms) for a total time of 8.6 min. Inversion recovery (IR-T_1) NMRI experiments employed sixty-four 13-s repetitions (TE = 10 ms; τ_{ir} = 0.0125, 0.025, 0.05, 0.1, 0.2, 0.4, 0.8, 1.6, 3.2, 6.4, and 12.8 s) for a total time of 19.3 h. (The long T_1 NMRI acquisition time was deemed necessary in order to perform a full multiple-exponential analysis.) Carr–Purcell–Meiboom–Gill (CPMG) T_2 NMRI experiments employed sixteen 4-s repetitions (20 echoes spaced 20 ms apart) for a total time of 17.1 min.

The procedure for obtaining T_2-sorted biofilm images is as follows. First, the 20 CPMG-T_2 NMRI echoes were Gaussian filtered, Fourier transformed, and phased to yield 20 real, increasingly T_2-weighted 2D NMR images. Next, pixel-by-pixel T_2 attenuation analysis employing a biexponential relax-

ation model yielded two T_2 relaxation time images (T_{2a} and T_{2b}) and their corresponding intensity coefficient images (I_{0a} and I_{0b}). Attenuation analysis involved an unconstrained nonlinear least-squares fit, employing a Levenberg–Marquardt algorithm (*18*).

Finally, a sorting routine (*19*) was used to resolve NMRI signal components based on their T_2 values, presumably corresponding to biofilm-associated and bulk water phases. The I_0:T_2 image pairs from the T_2 analysis were sorted with a predetermined threshold value *tdiv*. If T_{2i} ($i = a, b$) was less than *tdiv*, then its corresponding I_{0i} value was added to the biofilm image I_f, else it was added to the bulk water image I_w. Furthermore, intensities with a corresponding T_2 less than τ_{cp} were discarded as unreliable fitting values. Where possible, *tdiv* was determined from a histogram of all T_{2i} image pixel values, otherwise it was determined by trial and error.

T_1-sorted biofilm images were obtained by attenuation analysis and data sorting in a fashion analogous to the T_2 data. Conventional T_1-weighted NMRI data were processed by Gaussian filtering to reduce noise, followed by 2D Fourier transformation.

RESULTS AND DISCUSSION

Figure 2 compares a photograph with T_1-sorted biofilm, T_2-sorted biofilm, and conventional T_1-weighted NMR images for *E. coli* in a transparent bioreactor (Figs. 2a–2d, respectively; this reactor does not correspond with the schematic in Fig. 1). Conventional NMRI (Fig. 2d) clearly shows the entire fluid content of the reactor and the volume excluded by gas bubbles. (In these and subsequent figures, only the image pixels representing the model flow section are displayed, i.e., the images are cropped.) The bright circular features correspond with the fluid inlet and outlet lines, which protrude from the top plate. The portions of the tubes extending out of the image plane are not observed by NMRI. The inoculation port is seen as the diagonal line above the lower flow connection.

The T_1 and T_2-sorted biofilm NMRI (Figs. 2b and 2c, respectively) are in general agreement with the *true* biofilm distribution as shown in Fig. 2a, T_2-sorted NMRI showing better the lower density colonies. Both show a clean isolation of the biofilm-associated fluid phase. The sorting thresholds *tdiv* (determined by trial and error) were 2.2 and 0.1 s for the T_1 and T_2 images, respectively. T_1-sorted NMRI probably loses detail from extended diffusion exchange of water between bordering bulk and biofilm phases during the long T_1-sensitizing experiment time ($\tau_{ir} \propto T_1$), which is over an order of magnitude larger than for the T_2-sorted image ($\tau_{cp} \propto T_2$).

NMRI spatial resolution studies (*20*) (results not shown) were performed in which biofilm colonies were grown on agar plates for varying lengths of time. The colony dimensions (height and radius) were measured by both T_1-weighted NMRI and optical methods and compared. These experiments showed

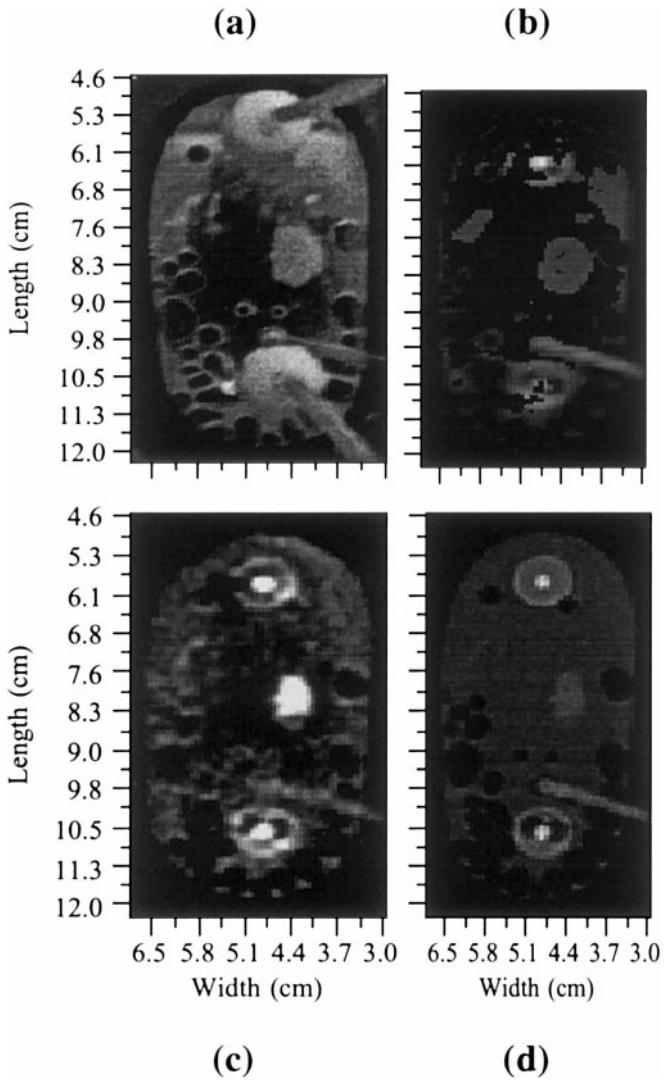

FIG. 2. Comparison of (a) optical, (b) T_1-sorted NMR, (c) T_2-sorted NMR, and (d) conventional NMR biofilm images for a bioreactor growth experiment (the reactor does not correspond with the schematic in Fig. 1).

that the biofilms are spatially resolved to the limits of the image pixel resolution.

Figures 3a and 3b compare a T_1-weighted NMR image of the parallel plate, open-flow bioreactor (Fig. 1) with an optical image. The distributors appear as high-intensity lines near the top and bottom of Fig. 3a because these locations contain more water. Main features are clearly visible in the NMRI, i.e., the biofilm colonies shown in gray, the flow channels swept of biofilm, and a few gas bubbles in the lower distributor.

Figure 3c shows a difference image created by subtracting binary optical and NMR images. (Binary NMRI and optical images were obtained from Figs. 3a and 3b, respectively, by selecting a minimum threshold intensity that yielded an image in visual agreement with the transparent model. The optical image resolution was reduced to match that of the NMR image.) Figure 3c shows false-positive biofilm locations in

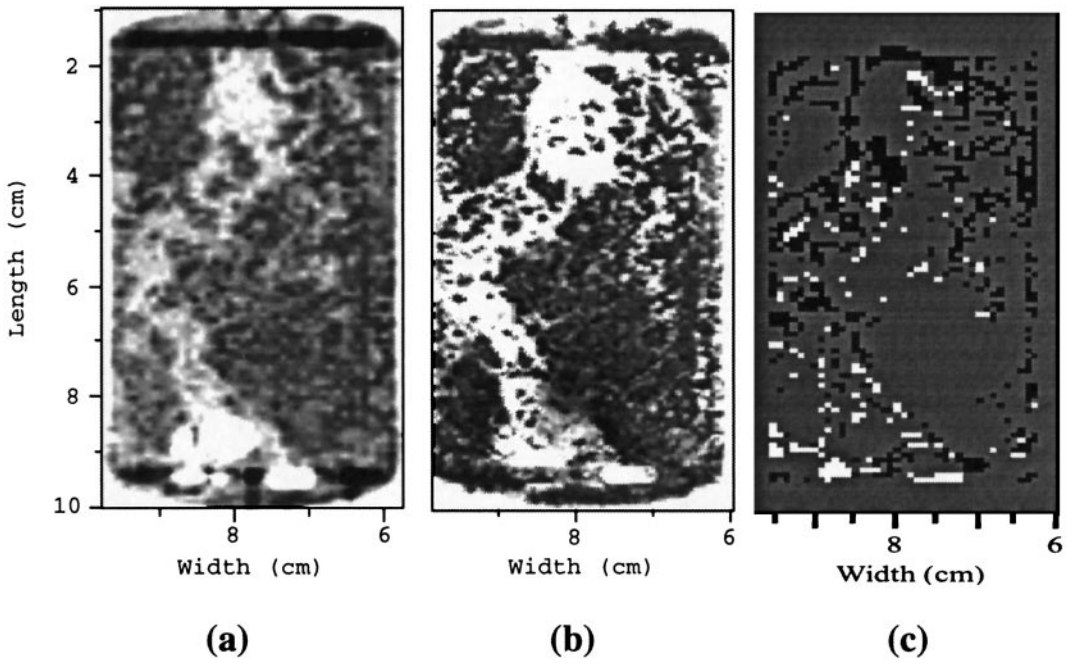

FIG. 3. Comparison of (a) T_1-weighted NMRI, (b) optical image, and (c) a binary difference image of a transparent bioreactor containing *E. coli* colonies grown in flowing nutrient. The T_1-weighted NMRI and the optical image agreed for 81% of the locations, with a net error of 12%.

black, false-negative locations in white, and locations in agreement with the optical image in gray. The NMRI and optical images agreed for 80.6% of the locations, with a net error of 12.0% false-negative locations.

Most of the discrepancy in Fig. 3c lies within the large channel and along the bioreactor walls, indicating possible image misregistration. Some detached and floating biomass in the large channel was redistributed when the sample was removed from the NMRI laboratory to take photographs. Further quantitative uncertainty was introduced by the marginal quality of both the optical and NMR images.

Figures 4a and 4b compare a T_1-weighted NMR image of biofilm in the glass-bead-packed bioreactor and an optical image of the same reactor after it was flooded with immersion liquid, respectively. A binary difference image (Fig. 4c) was created using the same method as in Fig. 3c. The NMRI and optical images agreed for 77.9% of the locations, with a net error of 8.1% false-negative locations. The images demonstrate that NMR imaging can rapidly and noninvasively detect the size, shape, and location of biofilm in a model saturated porous environment.

Figures 5a–5c compare T_2-sorted NMRI, optical, and difference images of biofilm in the glass-bead-packed bioreactor. The NMRI and optical images agreed for 82.3% of the locations, with a net error of 1.8% false-positive locations. Optical images were not as reliable for the bead-packed bioreactor, and close manual visual inspection showed biofilm not seen in the optical image. There appeared to be more biofilm in the reactor than indicated by the optical image and less than indicated by the NMR image.

Resolution of biofilm by T_1-weighted NMRI is partially dependent upon the *intensity threshold*, leading to a variable apparent biofilm boundary. In comparison, biofilm resolution by T_2-sorted NMRI depends upon a *relaxation time threshold tdiv*. With adequate T_2 resolution, *tdiv* can be determined from a histogram plot of T_2 image values. Contributions of overlapping fluid phases to a single pixel can be resolved with multiple-exponential analysis. The result is a more independent and complete isolation of biofilm-associated and bulk fluid signals.

Figure 6 shows the histogram of all (T_{2a} plus T_{2b}) image pixel values for an open-flow biofilm growth experiment. In a nonporous biofilm growth experiment, the histogram plots typically start out with a unimodal distribution representing bulk fluid. The histograms usually develop a bimodal distribution during the experiment, representing bulk and biofilm-associated fluid. Figure 7 shows the distribution of signal intensities over the same range of T_2 values plotted in Fig. 6, i.e., the summation of both I_{0a} and I_{0b} over their corresponding T_2 values. The area under the signal intensity curve can be used to determine the relative volumes of biofilm and bulk fluid.

Figure 8 shows the histogram of all T_{2a} and T_{2b} image pixel values for the porous biofilm growth experiment in Fig. 5a. The bulk and biofilm fluid phases were not clearly resolved with growth. The T_2 distribution has a reduced mean value and increased variance, due to pore surface relaxation in addition to

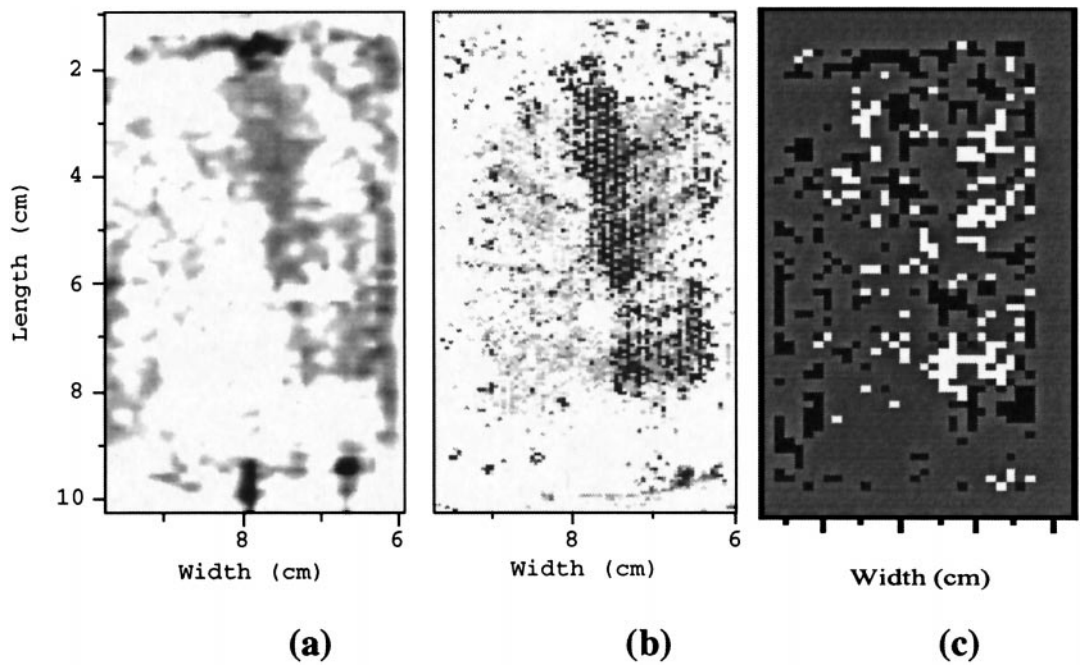

FIG. 4. Comparison of the (a) T_1-weighted NMRI, (b) optical image, and (c) binary difference image of the biofilm in the bead-packed bioreactor. The T_1-weighted NMRI and the optical image agreed for 78% of the locations, with a net error of 8.1%.

biofilm surface relaxation. This lack of phase resolution for T_2 experiments was a general trend in the porous systems, nevertheless Fig. 5a compares reasonably closely with the optical image.

Several NMR relaxation images were analyzed to determine a range of T_1 and T_2 values that represent bulk fluid (measured before biofilm growth) and biofilm-associated fluid. Table 1 shows these values for both the open-flow and bead-packed

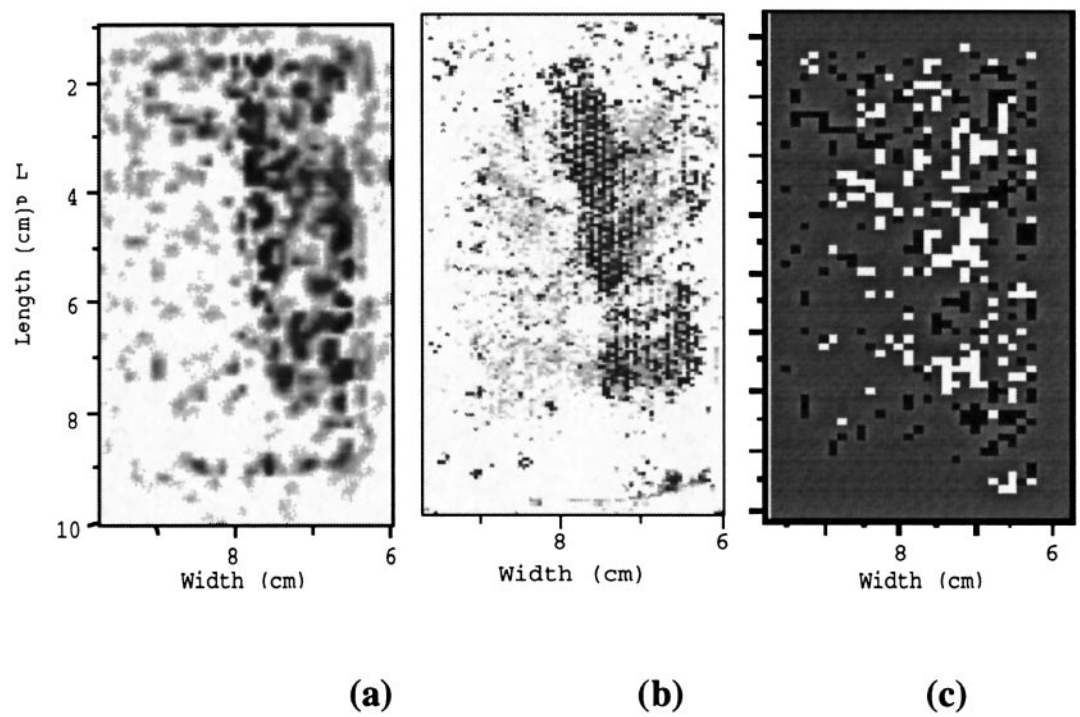

FIG. 5. Comparison of the (a) T_2-sorted NMRI, (b) optical image, and (c) binary difference image of the biofilm in the bead-packed bioreactor. The T_2-resolved NMRI and the optical image agreed in 82% of the locations, with a net error of 2%.

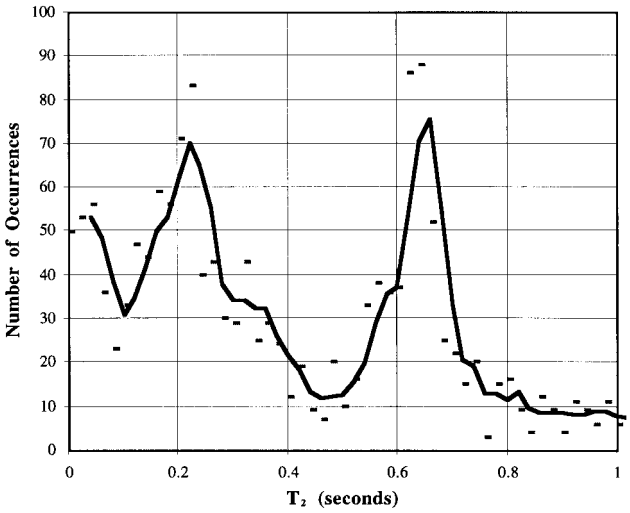

FIG. 6. Histogram of all T_2 image pixel values (biexponential model) for an open-flow biofilm growth experiment. The bimodal distribution reflects the presence of two distinct fluid phases (bulk and biofilm-associated water). The solid line represents the moving average of three consecutive data points.

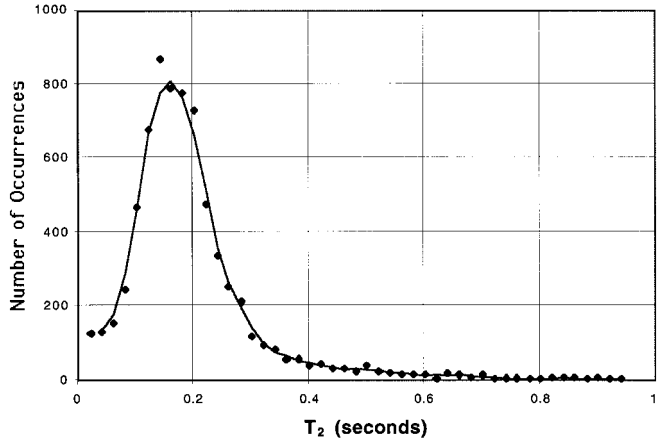

FIG. 8. Histogram of all T_2 values (biexponential model) for the porous growth experiment shown in Fig. 5. The bulk and biofilm-associated signal components are not resolved.

experiments. The bulk fluid T_2 values are approximately three times shorter in the bead-pack than in the open-flow experiment. The biofilm-associated T_1 and T_2 values each fall in similar ranges for both experiments. Nonimaging relaxation measurements of the bulk fluid showed some dependence upon the Luria broth nutrient concentration (T_1 = 2.2–2.9 s; T_2 = 0.81–1.12 s), both relaxation times decreasing with increasing concentration.

The selective imaging of biofilm in the presence of bulk water via sorted relaxation NMRI is subject to several conditions. Systems with a larger T_1 or T_2 contrast are easier to sort for a given experiment noise level. Clayden and Hesler (*21*) used simulations to show that a robust biexponential fit with a 10:1 ratio of T_2 times requires a signal-to-noise ratio of 10:1 or better. For a 2:1 ratio of T_2 times, a signal-to-noise ratio of 1000:1 or better was recommended.

Additionally, the biofilm-associated signal must be detected without distortion in the presence of the total signal plus noise, thus the NMR acquisition hardware must have adequate dynamic range (*22*). A 16-bit analog-to-digital converter is adequate for a M_f:M_o ratio $\approx$ 1:500, yielding a possible 128 intensity increments over M_f without distortion, where M_f and M_o are the biofilm and total time-domain NMR signal intensities, respectively. Other ways to ensure adequate dynamic range are to reduce M_o by avoiding excess bulk fluid in the image, e.g., by careful choice of image slice location, and by implementing T_1-weighting techniques to increase the M_f:M_0 ratio.

These conditions are more difficult to meet for biofilms in a porous medium, where the T_1 and T_2 relaxation time distributions are reduced and broadened by competing pore surface effects, and the signal is reduced by the excluded volume. T_1 differences are generally greater in the porous growth experiments, thus T_1-weighted and T_1-sorted methods are preferred. IR-T_1 experiments are prohibitively long, so T_1-weighted NMRI or possibly T_1-sorted imaging based upon saturation-recovery (*22*) methods is preferred for porous media biofilm growth studies.

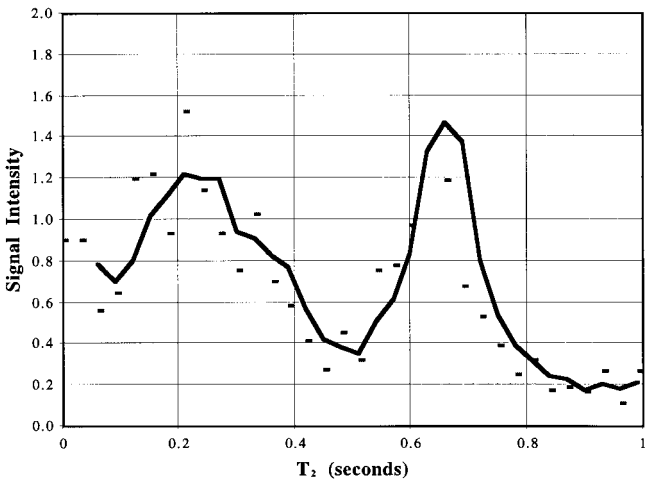

FIG. 7. Distribution of image intensities over T_2 image values for an open-flow biofilm growth experiment.

TABLE 1
NMR Imaging Relaxation Times for Biofilm-Associated and Bulk Water

Experiment	Fluid phase	T_1 (s)	T_2 (s)
Open-flow	Bulk	2.1–2.6	0.32–1.10
	Biofilm associated	0.3–1.9	0.07–0.50
Bead-pack	Bulk	0.5–2.5	0.12–0.40
	Biofilm associated	0.3–2.2	0.05–0.11

CONCLUSIONS

NMRI can be used for the selective, nondestructive detection and imaging of biofilms. The NMR-derived images are in general agreement with the optical images and with visual inspection of the transparent bioreactor. The phase resolution capability of relaxation NMRI is subject to relaxation time ratios, signal-to-noise ratio, and dynamic range considerations. A sorting method to separate fluid phases with relaxation time values approaching a 2:1 ratio was demonstrated. Where applicable, the additional processing effort is rewarded by a cleaner, more quantitative resolution of biofilm. T_1-based methods are preferred for porous media biofilm studies.

ACKNOWLEDGMENTS

This work was supported by Environmental Protection Agency Grant R821268. The authors thank Mr. Anthony Bermudez (UT Austin) for preparing the bioreactors and Ms. Anna Razatos for her help in microbiological matters.

REFERENCES

1. G. A. McFeters, *et al.,* Biofilm development and its consequences, in "Microbial Adhesion and Aggregation," (K. C. Marshall, Ed.), pp. 109–125, Springer-Verlag, New York (1984).
2. A. B. Cunningham, W. G. Characklis, F. Abedeen, and D. Crawford, Influence of biofilm accumulation on porous media hydrodynamics, *Environ. Sci. Technol.* **25,** 1305 (1991).
3. Y. M. Chen, L. M. Abriola, P. J. J. Alvarez, P. J. Anid, and T. M. Vogel, Modeling transport and biodegradation of benzene and toluene in sandy aquifer material: Comparisons with experimental measurements, *Water Resources Res.* **28,** 1833 (1992).
4. S. W. Taylor and P. R. Jaffé, Biofilm growth and the related changes in the physical properties of a porous medium 1. Experimental investigation, *Water Resources Res.* **26,** 2153–2159 (1990).
5. K. R. Brownstein and C. E. Tarr, Importance of classical diffusion in NMR studies of water in biological cells, *Phys. Rev. A* **19,** 2446–2453 (1979).
6. J. W. Pettegrew, "NMR, Principles and Applications to Biomedical Research," Springer-Verlag, New York (1989).
7. Z. Lewandowski, S. A. Altobelli, P. D. Majors, and E. Fukushima, NMR imaging of hydrodynamics near microbially colonized surfaces, *Water Sci. Technol.* **26,** 577–584 (1992).
8. Z. Lewandowski, S. A. Altobelli, and E. Fukushima, NMR and microelectrode studies of hydrodynamics and kinetics in biofilms, *Biotech. Prog.* **9,** 40–45 (1993).
9. Z. Lewandowski, P. Stoodley, S. A. Altobelli, and E. Fukushima, Hydrodynamics and kinetics in biofilm systems: Recent advances and new problems, *Water Sci. Technol.* **29,** 223–229 (1994).
10. Z. Lewandowski, P. Stoodley, and S. A. Altobelli, Experimental and conceptual studies on mass transport in biofilms, *Water Sci. Technol.* **31,** 153–162 (1995).
11. K. Potter, R. L. Kleinberg, E. W. McFarland, and F. J. Brockman, Assay for bacteria in porous media by diffusion-weighted NMR, *J. Magn. Reson. B* **113,** 9–15 (1996).
12. A. K. Stepp, R. S. Bryant, F. M. Llave, and R. P. Lindsey, Biopolymer system for permeability modification in porous media, *in* "Proceedings from the Fifth International Conference on Microbial Enhanced Oil Recovery and Related Biotechnology for Solving Environmental Problems," p 389–406 (1995).
13. T. C. Farrar and E. D. Becker, "Pulse and Fourier Transform NMR: Introduction to Theory and Methods," Academic Press, New York (1971).
14. W. E. Kenyon, Nuclear magnetic resonance as a petrophysical measurement, *Nucl. Geophys.* **6,** 153–171 (1992).
15. P. T. Callaghan, "Principles of Nuclear Magnetic Resonance Microscopy" Oxford Univ. Press, Oxford, UK (1991).
16. W. P. Rothwell and H. J. Vinegar, Petrophysical applications of NMR imaging, *Appl. Opt.* **24,** 3969–3972 (1985).
17. W. A. Edelstein, J. M. S. Hutchison, G. Johnson, and T. Redpath: Spin warp NMR imaging and applications to human whole-body imaging, *Phys. Med. Biol.* **25,** 751 (1980).
18. "Numerical Recipes in C: The Art of Scientific Computing, 2nd Ed.," (W. H. Press, *et al.* Eds.), Cambridge Univ. Press, Cambridge (1988).
19. P. D. Majors, P. Li and E. J. Peters, NMR imaging of immiscible displacements in porous media, *SPE Form. Eval.* **12,** 164–169 (1997).
20. L. Fevang, "Nuclear Magnetic Resonance Imaging of Biofilms and Bacterial Adhesion Studies," Thesis, The University of Texas at Austin, Austin, TX (1997).
21. N. J. Clayden and B. D. Hesler, Multiexponential analysis of relaxation decays, *J. Magn. Reson.* **98,** 271–282 (1992).
22. E. Fukushima and S. B. W. Roeder, "Experimental Pulse NMR: A Nuts and Bolts Approach," Addison-Wesley, Reading, MA (1981).